Comput Mech (2015) 55:287–302
DOI 10.1007/s00466-014-1101-6

ORIGINAL PAPER

A peridynamics–SPH coupling approach to simulate soil fragmentation induced by shock waves

Bo Ren · Houfu Fan · Guy L. Bergel · Richard A. Regueiro · Xin Lai · Shaofan Li

Received: 17 July 2014 / Accepted: 10 November 2014 / Published online: 6 December 2014

Abstract In this work, a nonlocal peridynamics–smoothed particle hydrodynamics (SPH) coupling formulation has been developed and implemented to simulate soil fragmentation induced by buried explosions. A peridynamics–SPH coupling strategy has been developed to model the soil–explosive gas interaction by assigning the soil as peridynamic particles and the explosive gas as SPH particles. Artificial viscosity and ghost particle enrichment techniques are utilized in the simulation to improve computational accuracy. A Monaghan type of artificial viscosity function is incorporated into both the peridynamics and SPH formulations in order to eliminate numerical instabilities caused by the shock wave propagation. Moreover, a virtual or ghost particle method is introduced to improve the accuracy of peridynamics approximation at the boundary. Three numerical simulations have been carried out based on the proposed peridynamics–SPH theory: (1) a 2D explosive gas expansion using SPH, (2) a 2D peridynamics–SPH coupling example, and (3) an example of soil fragmentation in a 3D soil block due to shock wave expansion. The simulation results reveal that the peridynamics–SPH coupling method can successfully simulate soil fragmentation generated by the shock wave due to buried explosion.

B. Ren · H. Fan · G. L. Bergel · S. Li (✉)
Department of Civil and Environmental Engineering, University of California, Berkeley, CA 94720, USA
e-mail: shaofan@berkeley.edu

R. A. Regueiro
Department of Civil, Environmental, and Architectural Engineering, University of Colorado at Boulder, Boulder, CO 80309, USA

X. Lai
Department of Engineering Structure and Mechanics, Wuhan University of Technology, Wuhan 430070, China

Keywords Explosion · Fragmentation · Peridynamics · Shock wave · SPH · Soil mechanics

1 Introduction

The numerical simulation of fracture and fragmentation in geomaterials induced by shock waves is a challenge in both computational failure mechanics and computational geomechanics. In order to accurately capture the physical process, there are several technical difficulties that need to be addressed: (1) strong discontinuities caused by crack initiation and evolution during the explosion process should be faithfully represented in numerical simulations; (2) the numerical model should correctly predict the interaction between soil and explosive gas, and (3) pressure and velocity must be accurately simulated along with the shock wave expansion front.

A decade ago, peridynamics emerged as an efficient nonlocal continuum theory that is capable of representing and capturing the discontinuous deformations in solids during fracture processes [1]. The original peridynamics model proposed by Silling [2] is a bond-based peridynamics method, which is an extension of atomistic bond-based molecular dynamics (MD) to a continuum level particle method. It uses pairwise bond force fields derived from certain macro-scale potential functions to represent the interactions between particles, similar to what is done in conventional MD simulations. The bond-based peridynamics method has been extensively used in predicting the damage and fracture processes in brittle materials [3], reinforced concrete materials [4], composite laminate structures [5], brazed joints [6], and modeling damages caused by impact loads [7]. However, there are some intrinsic drawbacks in the bond-based peridynamics method. Since the bond force vector is assumed to be

parallel to the deformation vector of each bond, this method will result in a fixed Poisson's ratio $\nu = 0.25$ due to the Cauchy-relation of material symmetries with respect to any orthogonal transformation, e.g. $D_{1122} = D_{1212}$. In fact, the constraint on Poisson's ratio poses a restriction on the method so that it cannot distinguish between distortional and volumetric deformation; thus it cannot accurately model incompressible plasticity.

To address the shortcomings of bond-based peridynamics, Silling et al. [8] proposed another version of peridynamics: the state-based peridynamics method. This method evaluates the bond force based on force states that are determined by the deformation states. A subset of this theory is called non-ordinary state-based peridynamics that uses constitutive correspondence to introduce classic constitutive models into the peridynamics framework [8,9]. In this theory, an approximation of the deformation gradient is constructed based on the geometrical information of the undeformed and deformed horizon (the compact support of a peridynamics particle).

Thus, the force state can be evaluated by using conventional elastic or elastoplastic constitutive models. Within constitutive correspondence, other phenomenological continuum models, such as damage models, can be introduced into the peridynamics framework as well [10]. State-based peridynamics has proven to be a very successful theory in predicting the fracture of solids. Using state-based peridynamics, Warren et al. [11] simulated the fracture of linear elastic and elasto-plastic materials; Foster et al. [12] tested the deformation of a viscoplastic bar under impact; Wecknera and Mohamed [13] implemented a stated-based viscoelastic peridynamics model, and Tuniki [14] applied state-based peridynamics to simulate fracture of concrete materials and structures.

Geomaterials, such as soil and rock, have pressure-sensitive inelastic behavior that dictates how the material responds under high pressure, which is present in shock wave loading. Over the past decades, many pressure-sensitive constitutive models for geomaterials have been developed. Examples include the Mohr–Coulomb (MC) plasticity model [15], the Matsuoka–Nakai (MN) plasticity model [16], and the Drucker–Prager (DP) plasticity model [17], among others. Recently, state-based peridynamics has been utilized to study the dynamic response of geo-materials and granular materials with pressure dependent constitutive models, e.g. [4,14,18,19]. To simulate the fragmentation of soil driven by high explosive (HE) gas, one has to develop a method that can capture the extremely high strain rate generated by the expansion of the explosive gas, as well as the interaction between the soil and the explosive gas. The expansion of the explosive gas will deform and distort the local soil configuration. Furthermore, some of the explosive gas particles will move into the soil to create a soil–gas interface. Thus, conventional mesh-based Lagrangian methods such as FEM will fail due to the severely distorted mesh. Moreover, it is very difficult to trace the fast-moving and evolving interface front by using conventional Eulerian mesh techniques such as the finite volume method [20].

In this work, a state-based peridynamics–SPH coupling approach is proposed to address the theoretical and numerical issues related to the fragmentation of soil under a high strain rate loading. The peridynamics method offers advantages in simulating fragmentation due to its ability to accurately simulate the fragmentation of soil. Additionally, smoothed particle hydrodynamics (SPH) [21] can handle the dynamic process of the explosive gas and trace the moving boundary intrinsically, because it is a Lagrangian particle method with an Eulerian kernel function [22].

This paper is organized in seven sections including this section: in Sect. 2, the equations of state-based peridynamics for soil under shock wave loading are presented; in Sect. 3, the peridynamic approximation is analyzed and the concept of virtual particles are introduced. In Sect. 4, the SPH equations for the explosive gas and the peridynamics–SPH coupling approach are presented. In Sect. 5, the non-linear constitutive update (DP model) under finite deformation and the related peridynamics formulations are discussed. In Sect. 6, several numerical examples are carried out to verify the proposed peridynamics–SPH coupling equations for the simulation of soil fragmentation. Finally, a few concluding remarks are made in Sect. 7.

2 State based peridynamics with artificial viscosity

Peridynamics can be used to simulate dynamic fracture, and it is particularly suitable for simulating complex fracture phenomena such as fragmentation. In this section, we will briefly discuss peridynamics discretization for solids.

A successful computational mechanics method has to accomplish two essential tasks: (1) Discretize the computational domain and represent the displacement field based on discrete points. In this regard, there are interpolation-based methods, such as the finite element method (FEM) [23,24] and several meshfree methods such as the reproducing kernel particle method (RKPM) [25–27], and collocation based methods, such as collocation of partial differential equations, or collocations of non-local integral equations, e.g. SPH. From the viewpoint of discretization, peridynamics is essentially a Lagrangian type of collocation method that discretizes the non-local force integration in the spatial domain [28]. (2) Assess and evaluate the derivative of the displacement field, i.e., the deformation gradient. This can be accomplished by taking derivatives of the interpolation functions as is done in FEM and RKPM , or constructing derivative kernel functions for the integral representation as is done in SPH.

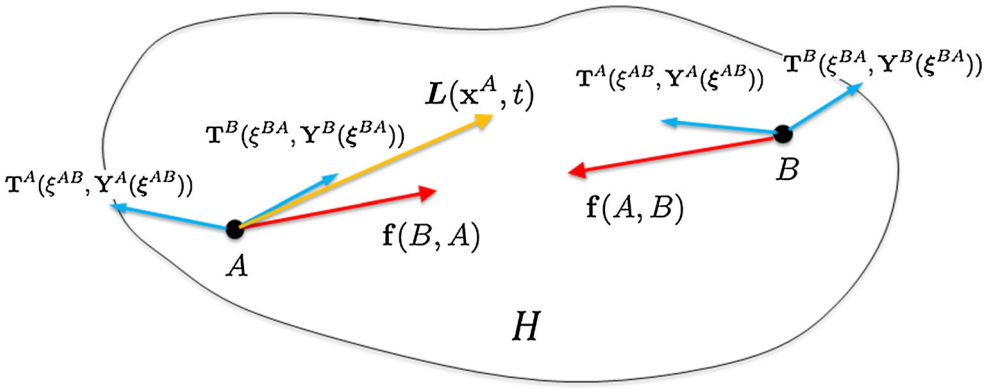

Fig. 1 Schematic illustration of the state-based peridynamics model

In the state-based peridynamics theory, each material medium is considered as a non-local continuum. Throughout this paper, a capital superscript, such as A, denotes a material medium, e.g., a peridynamic particle. Following the standard convention, capital variables with subscripts or capital dimensional indexes (X_I) refer to the quantities defined in the reference configuration, whereas the lower case variables with lower case subscripts (x_i) denote those in the current configuration. A material point $\mathbf{X}^A$ interacts with its neighboring particles within a certain distance δ. These neighboring particles form a region that is centered around $\mathbf{X}^A$, which is called the horizon [8]. All the neighboring particles are denoted as $\mathbf{X}^B$, $B = 1, 2 \ldots n_A$, where n_A is the total number of neighbors of particle A. We denote the horizon as $\mathcal{H}_{\mathbf{X}^A}$ as shown in Fig. 1. The peridynamics discretization has the typical topological structure of meshfree particle methods, e.g. [29]. The vector $\boldsymbol{\xi}^{AB} = \mathbf{X}^B - \mathbf{X}^A$ is defined as a bond vector of particle A; and all the kinematic interactions between particle A and B are represented through this bond, similar to the concept of an atomic bond in MD. The deformed bond $\boldsymbol{\xi}^{AB}$ is evaluated at the current configuration by the so-called deformation state function $\mathbf{Y}(\cdot)$,

$$\mathbf{Y}(\boldsymbol{\xi}^{AB}) := \mathbf{x}^B - \mathbf{x}^A = (\mathbf{X}^B - \mathbf{X}^A) + (\mathbf{u}^B - \mathbf{u}^A) = \boldsymbol{\xi}^{AB} + \boldsymbol{\eta}^{AB}, \tag{1}$$

where $\boldsymbol{\eta}^{AB} := \mathbf{u}^B - \mathbf{u}^A$. Moreover, we denote the scalar quantities,

$$\xi^{AB} = |\boldsymbol{\xi}^{AB}|, \quad \text{and} \quad \eta^{AB} = |\boldsymbol{\eta}^{AB}|\,. \tag{2}$$

The deformation state is local, therefore a given deformation bond can contribute to deformation states at both points A and B. We distinguish them as

$$\mathbf{Y}^A(\boldsymbol{\xi}^{AB}) \quad \text{or} \quad \mathbf{Y}^B(\boldsymbol{\xi}^{BA})\,.$$

In continuum mechanics, the equations of motion of a continuum with general dynamic motion are [23],

$$\rho_0 \ddot{\mathbf{u}} = \nabla_{\mathbf{X}} \cdot \mathbf{P}^T + \rho_0 \mathbf{b}, \tag{3}$$

where ρ_0 is the mass density of the solid in the reference configuration, $\nabla_{\mathbf{X}}$ denotes the divergence of the first Piola–Kirchhoff stress $\mathbf{P}$ with respect to the reference configuration, and $\mathbf{b}$ is the body force. In peridynamics, the above equation of balance of linear momentum is replaced by a non-local integral equation,

$$\rho_0 \ddot{\mathbf{u}} = \mathbf{L}(\mathbf{x}, t) + \rho_0 \mathbf{b}$$

where $\mathbf{L}(\mathbf{x}, t)$ is a non-local integration of force vector, $\mathbf{f}(\mathbf{x}, \mathbf{x}')$ (see Fig. 1), i.e.

$$\begin{aligned} \mathbf{L} &= \int_V \mathbf{f}\left(\mathbf{x}^A, \mathbf{x}^B\right) dV_{\mathbf{x}^B} \\ &= \int_{\mathcal{H}_{\mathbf{X}^A}} \Big[\mathbf{T}^A\left(\boldsymbol{\xi}^{AB}, \mathbf{Y}^A\left(\boldsymbol{\xi}^{AB}\right)\right) \\ &\qquad -\mathbf{T}^B\left(\boldsymbol{\xi}^{BA}, \mathbf{Y}^B\left(\boldsymbol{\xi}^{BA}\right)\right)\Big] dV_{\mathbf{X}^B} \end{aligned} \tag{4}$$

Therefore, the governing equation of state-based peridynamics [8] is,

$$\begin{aligned} \rho_0 \ddot{\mathbf{u}} = \int_{\mathcal{H}_{\mathbf{X}^A}} \Big[&\mathbf{T}^A\left(\boldsymbol{\xi}^{AB}, \mathbf{Y}^A\left(\boldsymbol{\xi}^{AB}\right)\right) \\ &-\mathbf{T}^B\left(\boldsymbol{\xi}^{BA}, \mathbf{Y}^B\left(\boldsymbol{\xi}^{BA}\right)\right)\Big] dV^B + \rho_0 \mathbf{b}, \end{aligned} \tag{5}$$

where $\mathbf{T}$ is the force-vector state. We would like to point out that the unit of the force state is N/m^3. Comparing Eq. (3) with Eq. (5), one can easily see that state-based peridynamics replaces the local divergence of the stress field with a non-local integral. Mathematically, the formula of the force state under constitutive correspondence is provided as,

$$\begin{aligned} &\mathbf{T} = \omega(|\boldsymbol{\xi}|)\mathbf{P} \cdot \boldsymbol{\xi} \cdot \mathbf{K}^{-1}, \quad \text{or in component form} \\ &T_i = \omega(|\boldsymbol{\xi}|) P_{iJ} \xi_K K^{-1}_{KJ}\,. \end{aligned} \tag{6}$$

where $\mathbf{K}$ is the shape tensor that is defined as

$$\mathbf{K} := \sum_{B \in \mathcal{H}_{\mathbf{X}^A}} \omega(|\boldsymbol{\xi}^{AB}|) \boldsymbol{\xi}^{AB} \otimes \boldsymbol{\xi}^{AB} \Delta V^B$$

In Eq. (5), $\mathbf{T}^A$ denotes the interaction force state from particle A to particle B through the bond $\boldsymbol{\xi}$, whereas $\mathbf{T}^B$ is the associated force state from particle B to particle A. In Eq. (6), $\mathbf{K}$ is the shape tensor, which will be discussed in the next section. In practice, the non-local integral in Eq. (5) is replaced by a finite summation,

$$\rho_0 \ddot{\mathbf{u}} = \sum_{B \in \mathcal{H}_{\mathbf{X}^A}} \left[\mathbf{T}^A \left(\boldsymbol{\xi}^{AB}, \mathbf{Y}^A \left(\boldsymbol{\xi}^{AB} \right) \right) - \mathbf{T}^B \left(\boldsymbol{\xi}^{BA}, \mathbf{Y}^B \left(\boldsymbol{\xi}^{BA} \right) \right) \right] \Delta V^B + \rho_0 \mathbf{b} \quad (7)$$

We may re-interpret Eqs. (6) and (7) as local meshfree difference operations representing the stress divergence term,

$$\begin{aligned} &\nabla \cdot \mathbf{P} = \frac{1}{\Delta \mathbf{X}} \cdot \Delta \mathbf{P}, \quad \text{where} \\ &\nabla \cdot \sim \frac{1}{\Delta \mathbf{X}} \cdot := \sum_{B \in \mathcal{H}_{\mathbf{X}^A}} \omega(|\boldsymbol{\xi}^{AB}|)(\cdot) \cdot \boldsymbol{\xi}^{AB} \cdot \mathbf{K}^{-1} \Delta V^B \\ &\qquad \text{and} \quad \mathbf{P} \sim \Delta \mathbf{P} := \mathbf{P}^A - \mathbf{P}^B \end{aligned} \quad (8)$$

The local meshfree difference operation interpretation of Peridynamics, which is based on the nonlocal integral equation, will be discussed in details in a separated paper. One may note that the non-ordinary state-based peridynamics formulation is material-specific, meaning that the peridynamics equation may change with different material constitutive models. This is certainly true for geomaterials as well because their state-based peridynamics formulation is generally different from that of a solid such as metals.

For the specific simulation of fracture or fragmentation of a solid induced by a shock wave, artificial damping must be considered in the numerical simulation in order to represent the transformation of kinetic energy into heat. This energy dissipation may be modeled as an artificial viscosity. In past decades, many artificial viscosity models have been proposed to capture the shock wave front such as [30]. In the SPH community, the Monaghan type of artificial viscosity models [31] are extensively used. However, these models were formulated to be suitable for SPH computations, e.g. Eqs. (24, 26 and 27). On the other hand, the peridynamics governing equation is based on the force state of each material particle, i.e. Eq. (5), and the peridynamics force state vectors are calculated based on the continuum mechanics stress tensor at the given particles, i.e. Eq. (6). Therefore, we need to add an artificial viscous stress in the peridynamics formulation as a shock capture term. To do so, we introduce a suitable Monaghan or von Neumann–Richtmyer type of artificial viscous stress in the peridynamics stress expression. First, we consider the artificial viscosity used in SPH by Liu and Liu [22],

$$\Pi^{AB} = \begin{cases} \dfrac{\left(-\alpha_\Pi \bar{c}^{AB} \phi^{AB} + \beta_\Pi \phi^{AB^2}\right)}{\bar{\rho}^{AB}}, & \mathbf{v}^{AB} \cdot \mathbf{x}^{AB} \le 0 \\ 0, & \mathbf{v}^{AB} \cdot \mathbf{x}^{AB} > 0 \end{cases} \quad (9)$$

where $\mathbf{x}$ is the position of the particle, and $\mathbf{v}$ is the particle velocity. The other variables are defined as follows,

$$\phi^{AB} = \frac{\delta^{AB} \mathbf{v}^{AB} \cdot \mathbf{x}^{AB}}{|\mathbf{x}^{AB}|^2 + \left(\varphi \delta^{AB}\right)^2} \quad (10)$$

$$\bar{c}^{AB} = \frac{1}{2}\left(c^A + c^B\right) \quad (11)$$

$$\bar{\rho}^{AB} = \frac{1}{2}\left(\rho^A + \rho^B\right) \quad (12)$$

$$\delta^{AB} = \frac{1}{2}\left(\delta^A + \delta^B\right) \quad (13)$$

$$\mathbf{v}^{AB} = \mathbf{v}^B - \mathbf{v}^A, \quad \mathbf{x}^{AB} = \mathbf{x}^B - \mathbf{x}^A \quad (14)$$

In the above equations, α_Π and β_Π are parameters that are set to be 1.0 [22]. $\varphi = 0.1$ is used to prevent numerical divergence when particle A and particle B are overlapped. c is the wave speed in the solid. δ^{AB} is the smoothing distance between particles A and B. Then we consider the following artificial Cauchy viscous stress,

$$\boldsymbol{\sigma}^{\text{viscous}} := \sum_{B \in \mathcal{H}_{\mathbf{X}^A}} \omega(|\boldsymbol{\xi}^{AB}|) \Pi^{AB} \mathbb{I} \, \Delta V_B \quad (15)$$

where $\mathbb{I}$ is the second order unit tensor. Eq. (15) may be viewed as the part of the Cauchy stress contributed by the artificial viscosity, which is evaluated in the current configuration. For the Lagrange description, we need a viscous stress tensor in the form of the first Piola–Kirchhoff stress as the measure of artificial viscosity, which is consistent with Eqs. (5) and (6), i.e.

$$\boldsymbol{\Theta}^{AB} = J \Pi^{AB} \mathbb{I} \cdot \mathbf{F}^{-T} \quad (16)$$

where $\mathbf{F}$ is the deformation gradient and $J = \det\{\mathbf{F}\}$. Then the calculation of the force state (Eq. (6)) with the artificial viscosity becomes,

$$\begin{aligned} &\mathbf{T} = \omega(|\boldsymbol{\xi}|)(\mathbf{P} - \Theta^{AB}) \cdot \boldsymbol{\xi} \cdot \mathbf{K}^{-1}, \quad \text{or} \\ &T_i = \omega(|\boldsymbol{\xi}|)(P_{iJ} - \Theta^{AB}_{iJ}) \xi_K K^{-1}_{KJ}. \end{aligned} \quad (17)$$

3 Peridynamics ghost particle enhancement

Non-ordinary state based peridynamics uses the approximate deformation state function to map a bond vector $\boldsymbol{\xi}$ from the reference configuration to the current configuration. The deformation state function $\mathbf{Y}(\boldsymbol{\xi})$ is a general function of $\boldsymbol{\xi}$. It is not necessarily a linear function of $\boldsymbol{\xi}$, nor does it have to be a continuous. Because the horizon of a particle is a compact supporting zone, the following Cauchy–Born rule is employed to represent the kinematic behavior of a bond,

$$\mathbf{Y}(\boldsymbol{\xi}) = \mathbf{F} \cdot \boldsymbol{\xi}, \tag{18}$$

where $\mathbf{F}$ is the approximate deformation gradient at a material point. Eq. (18) assumes that the deformed bond is a linear map of the original bond [32].

As mentioned in Sect. 2, an appropriate way to evaluate the gradient of displacement field, i.e., deformation gradient, is one of the important technical tasks of any computational mechanics method. State-based peridynamics constructs the shape tensor to represent the shape of the original horizon,

$$\mathbf{K} = \sum_{B \in \mathcal{H}_{\mathbf{X}^A}} \omega(|\boldsymbol{\xi}|) \boldsymbol{\xi} \otimes \boldsymbol{\xi} \, \Delta V^B \,. \tag{19}$$

Similar to Eq. (19), another matrix can be constructed to represent the shape of the deformed horizon:

$$\begin{aligned} \mathbf{N} &= \sum_{B \in \mathcal{H}_{\mathbf{X}^A}} \omega(|\boldsymbol{\xi}|) \mathbf{Y}(\boldsymbol{\xi}) \otimes \boldsymbol{\xi} \, \Delta V^B \\ &= \sum_{B \in \mathcal{H}_{\mathbf{X}^A}} \omega(|\boldsymbol{\xi}|) \mathbf{F} \cdot \boldsymbol{\xi} \otimes \boldsymbol{\xi} \, \Delta V^B \end{aligned} \tag{20}$$

In the above equation, $\mathbf{F}$ is in fact a local kinematic quantity, i.e. for each particle $\mathbf{X}^A$, $\mathbf{F}(\mathbf{X}^A)$ has a unique value. Therefore, it is constant in Eq. (20), and it may be taken out of the summation. Thus for a given material point $\mathbf{X}^A$, the deformation gradient can be evaluated explicitly from Eq. (20),

$$\mathbf{F} = \mathbf{N} \cdot \mathbf{K}^{-1} \,. \tag{21}$$

Equation (21) is a key step to construct the force state at every material point, because we can substitute it into all the available constitutive relations—elastic, elasto-plastic, or visco-plastic—to obtain the stress measure, and subsequently to calculate the force state $\mathbf{T}$.

To assess the accuracy of the peridynamics approximation to the gradient of the displacement fields, we measured the deformation gradient $\mathbf{F}$ in a uniform grid and a non-uniform grid under a prescribed linear deformation and bi-linear deformation,

$$x = 0.2X + 0.3Y + 0.4Z + 0.6, \quad \text{linear deformation} \tag{22}$$

$$x = 2.0X + 3.0Y + 4.0Z + 5.0XY + 6, \quad \text{bi-linear deformation.} \tag{23}$$

The numerical approximations and analytical solutions of the components of $\mathbf{F}$ ($F_{11} : \partial x/\partial X$, $F_{12} : \partial x/\partial Y$, $F_{13} : \partial x/\partial Z$) are listed in Tables 1 and 2 for a particle located at the boundary (No. 10) as well as one located inside the domain (No. 368), as shown in Fig. 2.

Recently, Bessa et al. [33] had investigated the link between meshfree state-based peridynamics and other meshfree methods such as RKPM. In fact, the peridynamics shape tensor is a special moment matrix in RKPM [34], and the discrete deformation gradient tensor in state-based peridynamics is a special case of hierarchical RKPM partition of unity interpolation discussed in [34]. Their work revealed that in the case of a uniform grid, the deformation gradient obtained from peridynamics can represent the MLS/RKPM deformation gradient analytically within the domain of interest. The results obtained in this work support the conclusion drawn in Bessa et al. (2014) [33]. The comparison reveals that state-based peridynamics can represent the linear deformation exactly with both uniform and non-uniform grids throughout the domain. For the bi-linear deformation, peridynamics can capture the exact results by using the uniform grid inside the domain of interests, although the accuracy of some solutions (F_{12}) deteriorate at the boundary.

As for the non-uniform grid shown in Fig. 2b, the numerical results are accurate inside the domain, with the error less than 1.15 %. The error may increase with highly irregular non-uniform mesh, and this error may increase to 30 % at the boundary. This phenomenon is a consequence of the particle deficiency problem. This issue stems from the fact that the particles near the boundary can only obtain force contributions from the particles inside the domain, and they lack contributions from outside of the domain.

Table 1 The deformation gradient at uniform grid

F	Boundary particle No. 10		Body particle No. 328	
	Peridynamics	Analytical	Peridynamics	Analytical
Linear deformation				
F_{11}	0.2	0.2	0.2	0.2
F_{12}	0.3	0.3	0.3	0.3
F_{13}	0.4	0.4	0.4	0.4
Bi-linear deformation				
F_{11}	72.0	72.0	57.0	57.0
F_{12}	18.1	13.0	13.0	13.0
F_{13}	4.0	4.0	4.0	4.0

Table 2 The deformation gradient at non-uniform grid

F	Boundary particle No. 10		Body particle No. 328	
	Peridynamics	Analytical	Peridynamics	Analytical
Linear deformation				
F_{11}	0.2	0.2	0.2	0.2
F_{12}	0.3	0.3	0.3	0.3
F_{13}	0.4	0.4	0.4	0.4
Bi-linear deformation				
F_{11}	76.9	77.3	60.6	59.9
F_{12}	24.5	15.6	44.2	43.8
F_{13}	4.0	3.3	4.0	3.9

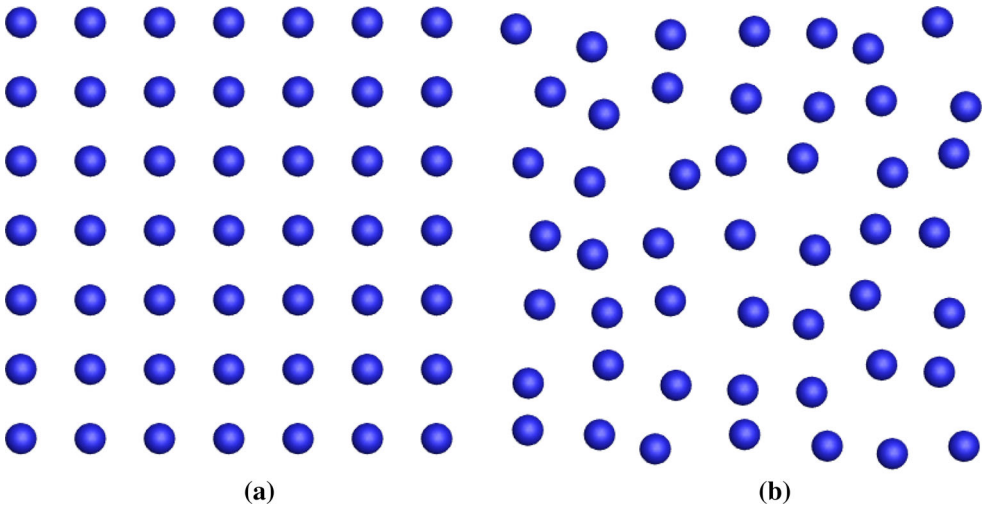

Fig. 2 The particle distribution. **a** Uniform grid; **b** non-uniform grid

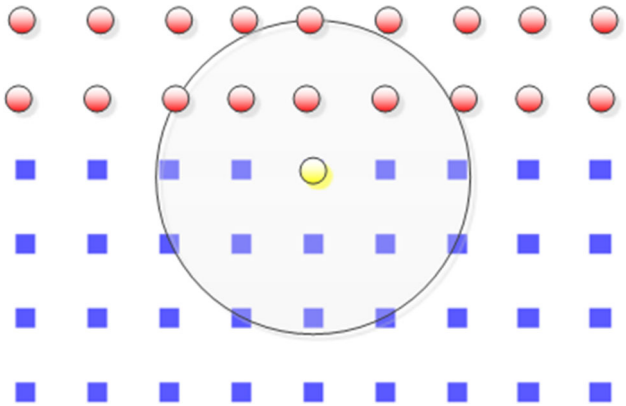

Fig. 3 Illustration of the virtual (*red*) and real (*blue*) peridynamic particles. (Color figure online)

The particle deficiency problem is a common issue for most particle methods such as SPH, RKPM, and MPM. In general, there are two approaches to deal with this type of problem: (1) add virtual particles near the boundary to fill up the compact support zone for the real particles located near the boundary of a simulation domain. This technique has been used in SPH, e.g. [35,36]; (2) derive the residual boundary terms that are due to breaking of the Kronecker Delta condition. This causes numerical interpolations to fail satisfying the essential boundary conditions, e.g. [37] in SPH simulations and [29] in RKPM computations. In this paper, we adopt a virtual particle enrichment method introduced by Liu and Liu [22] for SPH that is similar to the ghost particle technique adopted by Libersky et al. [35]. In this method, if a real particle A is located within a distance $2.0 \times \delta$ from the boundary, a virtual particle is placed symmetrically on the other side of the boundary. The virtual particles have the same material parameters as the real particles, as shown in Fig. 3. Here, the blue squares and red dots denote the real peridynamic particles and virtual peridynamic particles respectively. With the contribution from virtual particles, the accuracy of the numerical approximation for boundary particles will increase significantly so that it may match to that of the peridynamics approximation inside the simulation domain i.e. that of the bulk particles.

4 Peridynamics–SPH coupling technique

In this work, the main objective is to simulate soil fragmentation driven by the shock wave and explosive gas. In order to simulate the fracture process, we have first to know how to generate the shock wave, how to transfer the shock wave load from explosive gas to soil particles, and how to simulate shock wave propagation through the geomaterial medium. Physically, the explosion event experiences two coupling phases. The first one is the detonation phase, where the solid charge is converted into explosive gas with extremely high pressure. The second one is the expansion phase of the explosive gas. The detonation phase only takes less than a fraction of a second, whereas the explosive gas expansion process is a relative longer process. This process of shock wave propagation is accompanied by large deformation and fragmentation of soil particles and particle clusters. Since the whole explosion process takes less than a few seconds, it can generally be treated as an adiabatic and inviscid fluid–solid particle interaction process. Therefore, we neglect the effect of heat generation and heat transfer.

Since the explosive material is compressible, it experiences a change in volume and shape during the simulation. We adopt the SPH method to simulate the dynamic expansion of the explosive gas. SPH is a Lagrangian type of particle method that uses an Eulerian kernel. This property

gives the method advantages of fast computation times and accurate tracking of the shock wave front. During the explosion process, the explosive gas will move into the soil–gas interface thus creating highly inhomogeneous deformation along the shock wave front, which induces fragmentation of soil. This particular feature presents serious difficulties in modeling the explosive gas for both traditional mesh-based Lagrangian techniques, e.g. the Lagrangian type of FEM, as well as the Eulerian methods, e.g. the Eulerian type of FEM. The traditional Lagrangian FEM method would not work due to the severe distortion of the mesh. Additionally, the Eulerian type of FEM as well as FDM may not be able to track the fast-moving shock wave front without adopting additional techniques. Utilizing SPH to simulate the explosive gas will eliminate both of these issues thus producing more accurate and stable numerical results.

The SPH equations for the explosive gas are as follows,

$$\frac{D\rho^A}{Dt} = \sum_{B\in\mathcal{H}_{\mathbf{X}^A}} m^B(\mathbf{v}^B - \mathbf{v}^A)\cdot\nabla\omega^{AB} \tag{24}$$

$$\frac{D\mathbf{v}^A}{Dt} = -\sum_{B\in\mathcal{H}_{\mathbf{X}^A}} m^B\left(\frac{p^A}{\rho^{A2}} + \frac{p^B}{\rho^{B2}} + \Pi^{AB}\right)\nabla\omega^{AB} \tag{25}$$

$$\frac{De^A}{Dt} = \frac{1}{2}\sum_{B\in\mathcal{H}_{\mathbf{X}^A}} m^B\left(\frac{p^A}{\rho^{A2}} + \frac{p^B}{\rho^{B2}} + \Pi^{AB}\right)(\mathbf{v}^B - \mathbf{v}^A)\cdot\nabla\omega^{AB} \tag{26}$$

$$\frac{D\mathbf{x}^A}{Dt} = \mathbf{v}^A. \tag{27}$$

For further information, readers may consult [22] for details.

The governing equations for dynamic gases, i.e., Eqs. (24)–(26), are the continuity, momentum, and energy equations, respectively. In these equations, ρ, e, $\mathbf{v}$, t, and p are the gas density, internal energy, velocity vector, time, and pressure. Π^{AB} denotes the artificial viscosity, as shown in Eq. (9). We use the B-spline function as the SPH kernel function $\omega(x)$ [22] (the same kernel that is used for the state-based peridynamics method).

In this work, we adopt a (TNT) explosive charge model, and the pressure of the high explosive charge can be calculated by the equation of state of the following explosive gas model,

$$p = (\gamma - 1)\rho e, \tag{28}$$

where the factor γ is taken as 1.4 [22].

4.1 Peridynamic particles coupled with SPH particles

If we use SPH to simulate the soil, the inaccuracy of the SPH method may affect the accuracy and hence fidelity of the fragmentation simulation. Therefore, we adopt the peridynamics method to simulate the soil medium for its easy handling of fragmentation morphology, fast calculation, and reasonable accuracy. Now the focus of this approach is how to seamlessly couple the two methods: peridynamics (for soil) and SPH (for explosive gas).

In conventional computational mechanics, the interaction of two different media is called contact. There are two types of contact models: (1) the interpolation fields of the two different bodies are built up separately, i.e., two close particles in different bodies cannot contribute to the equations of motion of each other. The interactions between the two bodies are derived from the kinematic constraints at the interface, e.g. the geometric constraints at the contact interface. (2) A consistent single approximation field is constructed for multi-bodies, i.e., the equations of motion of the contact system are solved as a single system even though there are two different materials involved. This type of mixture contact algorithm is particularly suitable for meshfree particle methods.

In this work, we adopt the second approach because it simplifies the complex soil–explosive gas interaction. In this contact/coupling-approach, the soil and explosive gas are simulated by state-based peridynamics and SPH, respectively. However, an issue arises due to the fact that peridynamics uses the Lagrangian kernel whereas SPH uses the Eulerian kernel in the computation. Moreover, there is a buffer zone near the interface, which we call the "interphase zone." Since the coupling only occurs at the interphase of soil and explosive gas, we only need to set up a coupling strategy in the interphase area. In this work, the interphase zone is assumed to be located inside the computational domain, i.e., the explosive is fully surrounded by the soil. This assumption is true for most interaction problems, and it can avoid the complex interaction between interphase zone and boundary zone.

We first consider the force transfer mechanism from an SPH particle to a peridynamic particle. Suppose that there is a peridynamic particle A near the interphase whose horizon contains an SPH particle B. When we calculate the force state of the peridynamic particle A, we still use the peridynamics force state formula,

$$\mathbf{f}_{AB} = \mathbf{T}^A(\boldsymbol{\xi}^{AB}, \mathbf{Y}^A(\boldsymbol{\xi}^{AB})) - \mathbf{T}^B(\boldsymbol{\xi}^{BA}, \mathbf{Y}^B(\boldsymbol{\xi}^{BA}))$$

in which the only unknown is $\mathbf{T}^B(\boldsymbol{\xi}^{BA}, \mathbf{Y}^B(\boldsymbol{\xi}^{BA}))$, because the particle B is an SPH particle. In our peridynamics–SPH coupling scheme, we allow the contributions from both soil and explosive gas to interact with the soil particle A as shown in Fig. 4. This means that the peridynamic particles can "feel" the SPH particle across the interphase, likewise the SPH particles can "feel" the peridynamic particles. Therefore, inside the interphase zone, an SPH particle located in the horizon of a peridynamic particle will be considered a "peridynamic" particle, and it is used to calculate the force state vector of the original peridynamic particle (see Eq. (6)).

The key of this interphase procedure is the method in which to calculate force state $\mathbf{T}^B(\boldsymbol{\xi}^{BA}, \mathbf{Y}^B(\boldsymbol{\xi}^{BA}))$. First,

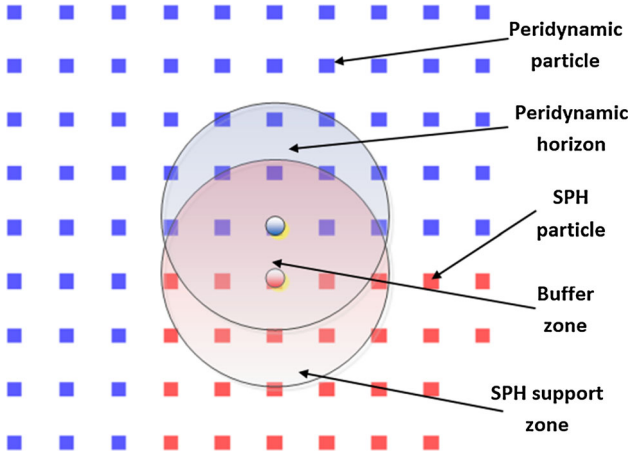

Fig. 4 The peridynamics and SPH coupling: peridynamics particles (*blue*) and SPH particles (*red*). (Color figure online)

SPH uses the Eulerian kernel function, which can be rebuilt in real time in the soil–gas particle interphase. Second, we always know the pressure of the SPH particle because $p^B = (\gamma - 1)\rho^B e$. In fact, Eq. (17) implies that the force state calculation is implemented in the reference configuration, and is associated with the first Piola–Kirchhoff stress. Given that the explosive gas is treated as an inviscid flow, we choose the Cauchy stress of an SPH particle as its hydrostatic pressure,

$$\sigma_{ij}^B = p^B \delta_{ij} \tag{29}$$

Once the Cauchy stress is known, we can calculate the force state at point B. It is well known that the first derivative calculation using SPH is often inaccurate. Instead of using the SPH approximation, we construct a second order structure tensor at the current configuration with the Eulerian kernel function:

$$\begin{aligned}\mathbf{M} &= \sum_{A\in\mathcal{H}_{\mathbf{x}^B}} \omega(\mathbf{x}^B)\mathbf{Y}(\boldsymbol{\xi}^{BA}) \otimes \mathbf{Y}(\boldsymbol{\xi}^{BA})\Delta V^B \\ &= \sum_{A\in\mathcal{H}_{\mathbf{x}^B}} \omega(\mathbf{x}^B)\mathbf{x}^{BA} \otimes \mathbf{x}^{AB}\Delta V^A \end{aligned} \tag{30}$$

Then the force state of the SPH particle B in the interphase zone can be evaluated as:

$$\begin{aligned}&\mathbf{T}^B = \omega(\mathbf{x}^B) J\boldsymbol{\sigma}^B \cdot \mathbf{M}^{-1} \cdot \mathbf{Y}(\boldsymbol{\xi}^{BA}), \quad \text{or} \\ &T_i^B = \omega(\mathbf{x}^B) J\sigma_{ij}^B M_{jk}^{-1} Y_k(\xi^{BA}).\end{aligned} \tag{31}$$

where $J = \det\mathbf{F}$. The force state shown above is derived from the principle of virtual work. Considering that the variation in the external virtual work is equal to the variation in the displacement $\delta\mathbf{Y}(\boldsymbol{\xi})$ dotted with the force vector, one may solve for the force state $\mathbf{T}$. In this scenario, we use the Kirchhoff stress $\boldsymbol{\tau} = J\boldsymbol{\sigma}$, and the Almansi strain $\boldsymbol{e} = \frac{1}{2}(\mathbb{I} - \mathbf{b}^{-1})$ as conjugate pairs in the internal virtual work term.

Another advantage of this coupling approach is that it resolves the boundary deficiency problem of particle methods. The soil–gas interphase is replaced by an interphase zone in which the compact supports of both soil and gas particles are filled with the particles of their own phase, and the particles of the other as "virtual" particles of their respective phase.

4.2 SPH particles coupled with peridynamic particles

A similar situation to that mentioned above occurs when a peridynamic particle is located inside the support zone of an SPH particle.

When we calculate the interaction force that acts on an SPH particle but is induced by a peridynamic particle, we consider the peridynamic particle as an SPH particle. Therefore, it participates in the calculation of every conservation law of that SPH particle. For example, for the SPH particle A, its linear momentum equation reads as,

$$\frac{D\mathbf{v}^A}{Dt} = -\sum_{B\in\mathcal{H}_{\mathbf{x}^A}} m^B \left(\frac{p^A}{\rho^{A^2}} + \frac{p^B}{\rho^{B^2}} + \Pi^{AB}\right)\nabla\omega^{AB}\,. \tag{32}$$

Assume that there is a particular particle B that is a peridynamic particle. It is obvious that most properties of the peridynamic particle B are known. For instance, the mass and density of the peridynamic particle B are constant during the computation. When calculating Eq. (32), we only need to know what p^B is. In the peridynamics–SPH coupling strategy, we set

$$p^B = \sigma_{ij}^B \delta_{ij}, \tag{33}$$

where σ_{ij}^B is the Cauchy stress of the peridynamic particle B. This stress tensor can then be evaluated by the standard procedure of state-based peridynamics.

In general, the contact/interaction model introduced here may lead to nonphysical inter-particle penetration near the interphase. This penetration happens not only between the peridynamic and SPH particles, but also among the first layers of the peridynamic particles. There are several numerical treatments to solve this problem, for example, the penalty force method [22]. We can apply penalty terms on the adjacent particles near the interface to prevent the inter-particle penetration between two adjacent media. However, this technique cannot be applied to solve the nonphysical inter-particle penetration that occurs inside the soil. To overcome this difficulty, an artificial viscosity function is introduced. The artificial viscosity function (Eq. (9)) not only stabilizes the numerical calculation of the shock wave, it also prevents the inter-particle penetrations. In this work, the same Monaghan type artificial viscosity function presented in Eq. (9) is used in the computation,

$$\Pi^{AB} = \begin{cases} \frac{-\alpha_\Pi \bar{c}^{AB}\phi^{AB} + \beta_\Pi \phi^{AB\,2}}{\bar{\rho}^{AB}}, & \mathbf{v}^{AB}\cdot\mathbf{x}^{AB} \le 0 \\ 0, & \mathbf{v}^{AB}\cdot\mathbf{x}^{AB} > 0 \end{cases} \tag{34}$$

The components of the above equation are the same as those of the peridynamics artificial viscosity. The parameters here are chosen as $\alpha_\Pi = 1$ and $\beta_\Pi = 2$ for most cases. However, these values are not large enough to prevent the inter-particle penetration induced by the shock wave. In this work, $\beta_\Pi = 10$ is used in the computation.

5 Drucker–Prager model and constitutive update

The peridynamics method uses a unique approach that approximates the deformation gradient, and it relates this discrete version of deformation gradient to stress measures in conventional continuum mechanics (Eq. (21)). Therefore, the conventional constitutive models and their numerical implementation algorithms can be used to evaluate the stress fields ($\boldsymbol{\sigma}$ or $\mathbf{P}$) of the peridynamics domain. Soil materials generally exhibit non-linear behavior after yield. Moreover, its yield surface is pressure sensitive [17]. Even though the inelastic behavior of soil is extremely complex in three-dimensional space, many successful constitutive models were developed for soil, such as the Mohr–Coulomb (MC) model, Matsuoka–Nakai (MN) model, and Drucker–Prager (DP) model. In this work, we use the Drucker–Prager plasticity model [17] for the soil, and we implement it alongside the peridynamics formulation. The Drucker–Prager model uses a smooth approximation of the MC yield criterion to determine the yield surface of the soil. Moreover, the parameters of the DP model are well calibrated with experimental tests [38]. The DP model and its updated versions are extensively used in numerical simulations of soil, rock, and concrete structures [39].

In this section, the peridynamics equations for updating a non-linear constitutive model with finite deformation are derived. Formally, the DP yield function is expressed as:

$$\begin{aligned} f &= \|\mathbf{s}\| - (A^\phi c - B^\phi p) \le 0 \\ A^\phi &= \frac{2\sqrt{6}\cos\phi}{3+\beta\sin\phi} \\ B^\phi &= \frac{2\sqrt{6}\sin\phi}{3+\beta\sin\phi} \quad -1 \le \beta \le 1 \end{aligned} \tag{35}$$

where $\mathbf{s}$ is the deviatoric stress, c the cohesion (P_a), ϕ the friction angle, and p is the mean Cauchy stress. When $\beta = 1$, the DP model approximates the MC model at the triaxial extension (TE) corner; $\beta = -1$ represents an approximation of the MC model at the triaxial compression (TC) corner [40]. The non-associative plastic potential function can be written as:

$$\begin{aligned} g &= \|\mathbf{s}\| - (A^\psi c - B^\psi p) \\ A^\psi &= \frac{2\sqrt{6}\cos\psi}{3+\beta\sin\psi} \\ B^\psi &= \frac{2\sqrt{6}\sin\psi}{3+\beta\sin\psi} \quad -1 \le \beta \le 1 \end{aligned} \tag{36}$$

where ψ denotes the dilation angle. In the case of $\phi = 0$, $\psi = 0$, Eqs. (35) and (36) can reduce to a form similar to J_2 plasticity. The Helmholtz free energy function $\rho\Psi$ per unit deformed volume can be separated into elastic and plastic parts:

$$\rho\Psi(\boldsymbol{\epsilon}^e, \boldsymbol{\zeta}) = \frac{1}{2}\boldsymbol{\epsilon}^e : \mathbf{D}^e : \boldsymbol{\epsilon}^e + \frac{1}{2}\boldsymbol{\zeta}\cdot\mathbf{H}\cdot\boldsymbol{\zeta} \tag{37}$$

where $\boldsymbol{\epsilon}^e$, $\mathbf{D}^e$, and $\mathbf{H}$ are the elastic strain tensor, elastic modulus tensor, and hardening/softening matrix, respectively. $\boldsymbol{\zeta}$ is a set of kinematic internal state variables (ISVs) associated with kinematic plastic hardening/softening involved in the geo-constitutive models [40]. From Eq. (37), the rate equations of the stress state ($\boldsymbol{\sigma}$) and ISV ($\mathbf{q}^\zeta$) can be derived as,

$$\dot{\boldsymbol{\sigma}} = \frac{\partial(\rho\Psi)}{\partial\dot{\boldsymbol{\epsilon}}^e} = \mathbf{D}^e : \dot{\boldsymbol{\epsilon}}^e = \mathbf{D}^e : (\dot{\boldsymbol{\epsilon}} - \dot{\boldsymbol{\epsilon}}^p) \tag{38}$$

$$\dot{\mathbf{q}}^\zeta = \frac{\partial(\rho\Psi)}{\partial\dot{\boldsymbol{\zeta}}} = \mathbf{H}\cdot\dot{\boldsymbol{\zeta}} \tag{39}$$

In this work, we choose the internal variables of the soil $\mathbf{q}^\zeta$ as: $\mathbf{q}^\zeta = \{c, \phi, \psi\}^T$. To simplify the problem, this paper treats ϕ and ψ as parameters, and $\mathbf{q}^\zeta = \{c\}$. We assume that c has linear hardening/softening modulus, H. From the plastic potential function (Eq. (36)), the evolution of plastic flow becomes,

$$\begin{aligned} \dot{\boldsymbol{\epsilon}}^p &= \dot{\gamma}\frac{\partial g}{\partial\boldsymbol{\sigma}} = \dot{\gamma}\left(\frac{\partial\mathbf{s}}{\partial\boldsymbol{\sigma}} + B^\psi\frac{\partial p}{\partial\boldsymbol{\sigma}}\right) \\ &= \dot{\gamma}\left(\hat{\mathbf{n}} + \frac{1}{3}B^\psi\mathbb{I}\right) \end{aligned} \tag{40}$$

where $\hat{\mathbf{n}}$ is the normal vector of the deviatoric stress, and $\mathbb{I}$ is the second order unit tensor. The evolution equation of the ISV is defined as:

$$\dot{c} = H\cdot\dot{\zeta} = \dot{\gamma}H\cdot h(\boldsymbol{\sigma}, c) \tag{41}$$

Based on the principle of maximum plastic dissipation, we have

$$h = -\frac{\partial f}{\partial c} = A^\phi \tag{42}$$

$\dot{\gamma}$ can be solved from the consistency condition $\dot{f} = 0$:

$$\begin{aligned} \dot{\gamma} &= \frac{1}{\chi}\frac{\partial f}{\partial\boldsymbol{\sigma}} : \mathbf{D}^e : \dot{\boldsymbol{\epsilon}} \\ \chi &= \frac{\partial f}{\partial\boldsymbol{\sigma}} : \mathbf{D}^e : \frac{\partial g}{\partial\boldsymbol{\sigma}} - \frac{\partial f}{\partial c}\cdot H\cdot h \end{aligned} \tag{43}$$

Equations (38), (39) and (43) are the standard equations for the constitutive update of a non-linear plastic soil model. There are three sets of unknowns $(\boldsymbol{\sigma}, c, \gamma)$ coupled in the non-linear equations. These can be solved by using the

Newton–Raphson method [23]. In this work, the following simple explicit updating algorithm is implemented,

$$\boldsymbol{\sigma}_{n+1}^{tr} = \boldsymbol{\sigma}_n + \mathbf{D}^e : \Delta\boldsymbol{\epsilon} \tag{44}$$

$$f_{n+1}^{tr} = \|\mathbf{s}^{tr}\| - (A^{\phi_n} c_n - B^{\phi_n} p_{n+1}^{tr}) \tag{45}$$

if $f_{n+1}^{tr} < 0$ elastic phase: updating $\boldsymbol{\sigma}_{n+1}$ and c.
if $f_{n+1}^{tr} \geq 0$ plastic phase:

$$\Delta\gamma = \frac{f_{n+1}^{tr}}{2\mu + K B^{\phi} B^{\psi} + H(A^{\phi})^2} \tag{46}$$

$$\boldsymbol{\sigma}_{n+1} = \boldsymbol{\sigma}_{n+1}^{tr} - \Delta\gamma(K B^{\psi} \mathbb{I} + 2\mu\hat{\mathbf{n}}_{n+1}) \tag{47}$$

$$c_{n+1} = c_n + \Delta\gamma H \cdot h(\boldsymbol{\sigma}, c) \tag{48}$$

Equation (44) is the formula used for calculating the trial stress under the assumption of small deformation. However, the damage process is in general associated with finite deformation. Under finite deformation, Eq. (44) should be replaced with nonlinear equations based on the Hughes–Winget algorithm [41]. During finite deformations, the motion of a material volume element in any time increment consists of both a deformation and a rotation. To measure objective kinematic deformation, a configuration at time step $n + \alpha$ is defined,

$$\mathbf{x}^{n+\alpha} = (1 - \alpha)\mathbf{x}^n + \alpha\mathbf{x} \tag{49}$$

In this work, we choose the parameter $\alpha = 0.5$. Similar to Eq. (23), which approximates the deformation gradient in state-based peridynamics, the deformation gradient at configuration $\mathbf{x}^{n+\alpha}$ can be derived as,

$$\mathbf{L} = \frac{\partial \mathbf{x}^{n+\alpha}}{\partial \mathbf{X}} = \left[\sum_{B \in \mathcal{H}_{\mathbf{x}^A}} \omega(|\boldsymbol{\xi}|)(\mathbf{x}^{B,n+\alpha} - \mathbf{x}^{A,n+\alpha}) \otimes \boldsymbol{\xi}\right] \cdot \mathbf{K}^{-1} \tag{50}$$

Meanwhile, the gradient of the displacement increment $\Delta\mathbf{u}$ with respect to the reference configuration can be written as,

$$\mathbf{C} = \frac{\partial \Delta\mathbf{u}}{\partial \mathbf{X}} = \left[\sum_{B \in \mathcal{H}_{\mathbf{x}^A}} \omega(|\boldsymbol{\xi}|)(\Delta\mathbf{u}^B - \Delta\mathbf{u}^A) \otimes \boldsymbol{\xi}\right] \cdot \mathbf{K}^{-1} \tag{51}$$

Therefore, the gradient of $\Delta\mathbf{u}$ at the configuration $(\mathbf{x}^{n+\alpha})$ can be obtained as,

$$\mathbf{G} = \frac{\partial \Delta\mathbf{u}}{\partial \mathbf{x}^{n+\alpha}} = \mathbf{C} \cdot \mathbf{L}^{-1} \tag{52}$$

where $\mathbf{G}$ is the incremental deformation gradient. It can be split into the strain and rotation increment parts respectively,

$$\boldsymbol{\Gamma} = (\mathbf{G} + \mathbf{G}^T)/2 \tag{53}$$

$$\boldsymbol{\Omega} = (\mathbf{G} - \mathbf{G}^T)/2 \tag{54}$$

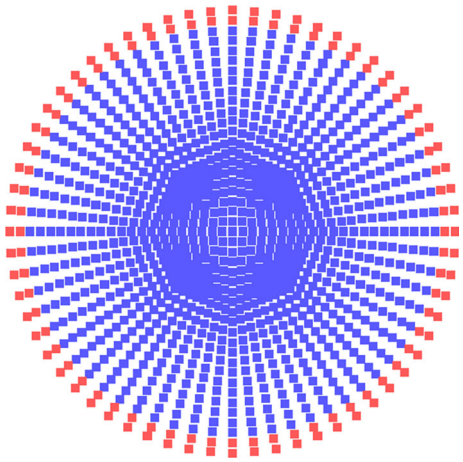

Fig. 5 The expansion of explosive gas

The objective stress increment can be calculated,

$$\Delta\boldsymbol{\sigma} = \mathbf{D}^e : \boldsymbol{\Gamma} \tag{55}$$

Finally, the constitutive update equation (Eq. (44)) is replaced by,

$$\boldsymbol{\sigma}^{n+1} = \hat{\boldsymbol{\sigma}}^n + \Delta\boldsymbol{\sigma} \tag{56}$$

$$\hat{\boldsymbol{\sigma}}^n = \mathbf{R}^T \cdot \boldsymbol{\sigma}^n \cdot \mathbf{R} \tag{57}$$

$$\mathbf{R} = \mathbb{I} + (\mathbb{I} - \alpha\boldsymbol{\Omega})^{-1} \cdot \boldsymbol{\Omega}. \tag{58}$$

6 Numerical simulations

In this section, we present three numerical examples by using the coupled peridynamics and SPH approach. For the buried explosive problem, the first technical concern is to simulate the evolution of the explosive gas. In the first example, we simulate the expansion of the explosive gas in an ambient space that is initially packed in a cylinder. Since the cylinder is axisymmetric, this problem can be reduced to a 2D problem.

6.1 Simulation of 2D explosive gas expansion using SPH

In this example, we assume that the detonation speed of the HE (TNT) is infinite. Consequently, only the expansion of the explosive gas is predicted by the SPH method. This example is carried out to validate the further explosive loading generated in the underground explosion. To compare with the numerical results from commercial software (MSC Dytran), we assume that the explosive gas is placed in a vacuum space. The radius of the TNT explosive gas is 0.1 m. As discussed in Sect. 3, the SPH method needs an enrichment near the boundary to improve the computational accuracy. In this work, the virtual particles approach described by Liu and Liu [22] is implemented. The computational model is shown in Fig. 5. The blue cubes are explosive gas (SPH) particles, and the

red cubes are virtual SPH particles with the same density and energy as the TNT gas. The computational domain is discretized into 1,057 SPH particles and 138 virtual particles. The initial material parameters for the TNT gas are: $\rho = 1,630\,\text{kg/m}^3$ and $e = 4.29 \times 10^6\,\text{J/kg}$. The equation of state (EOS) of the ideal gas is used, and the parameter $\gamma = 1.4$. The coefficients of the artificial viscosity are chosen as $\alpha_\Pi = 1.0$, $\beta_\Pi = 10.0$, and $\phi = 0.1$. The simulation time step is $\Delta t = 5.0 \times 10^{-7}\,\text{s}$.

Because the explosive gas is treated as inviscid, the explosion performs as a blast wave resulting from the pressure of the gas. This means that the evolution of the pressure field is a very important quantity during the simulation. Here, the pressure transients along the radial direction are plotted (Fig. 6) alongside those that were calculated from MSC/Dytran [22]. MSC/Dytran is a grid-based hydrocode, in which the results are interpolated with volumes of cells. One can find that the pressure curves from Dytran decrease smoothly to zero. In contrast, SPH results are associated with particles that have no pressure data existing beyond the gas front. The comparison indicates that the SPH equations used here can predict the pressure evolution with great accuracy.

The dynamic expansion sequences are plotted in Fig. 7 with contours of pressure (mean stress). From these plots, one can find the explosive expands symmetrically along the radial direction, as is expected.

6.2 The 2D peridynamics–SPH coupling case

Once the explosive gas starts to expand, it will interact with the surrounding soil thus exerting pressure and causing the soil to fracture. This process is usually very fast because the explosive gas wave front moves as a shock wave in geomaterials. Therefore, the second technical concern is the soil–gas interaction and the subsequent fragmentation of soil.

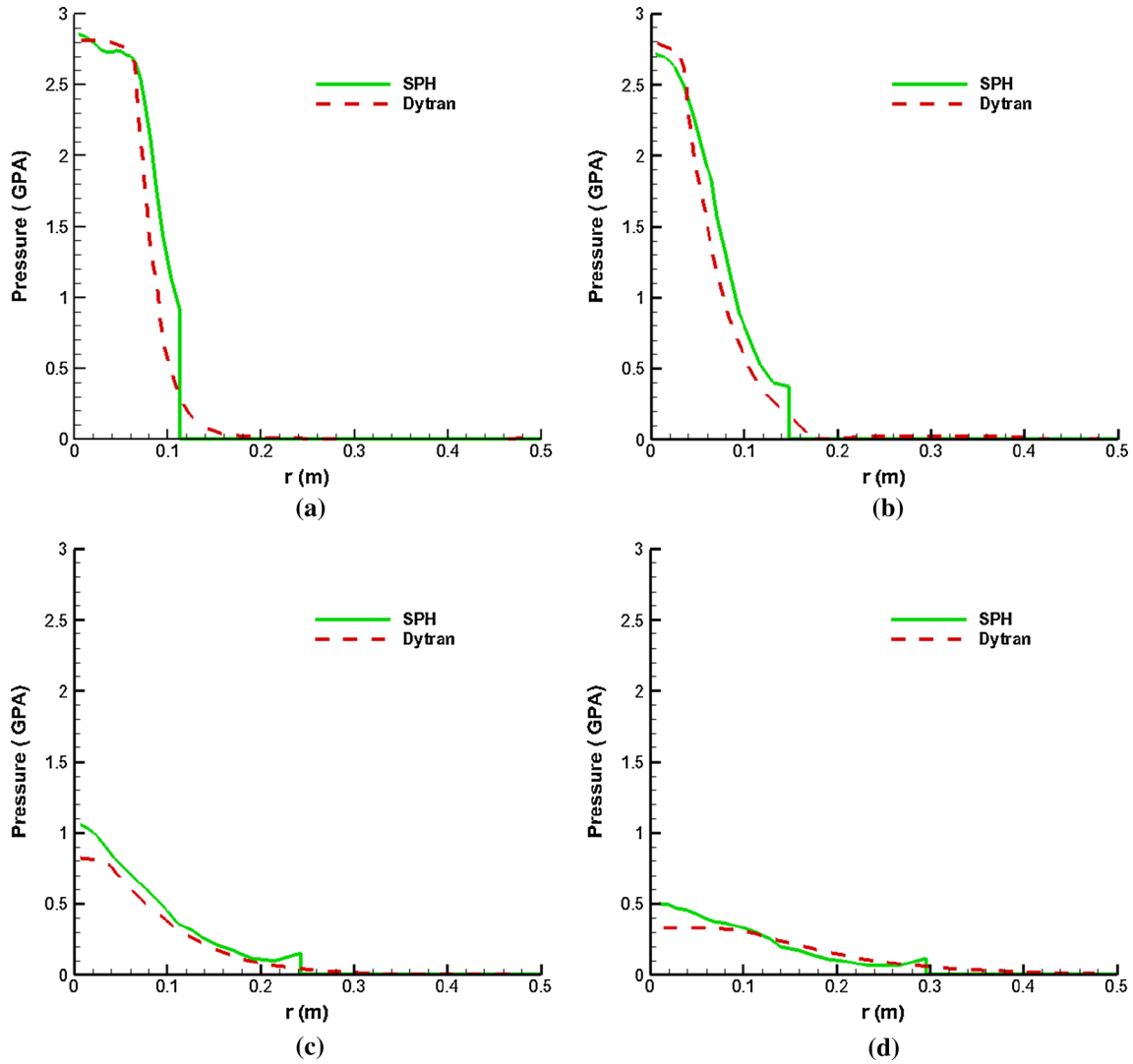

Fig. 6 The pressure evolution of HE (TNT) gas by SPH and Dytran. **a** $t = 0.02\,\text{ms}$; **b** $t = 0.04\,\text{ms}$; **c** $t = 0.08\,\text{ms}$; **d** $t = 0.10\,\text{ms}$

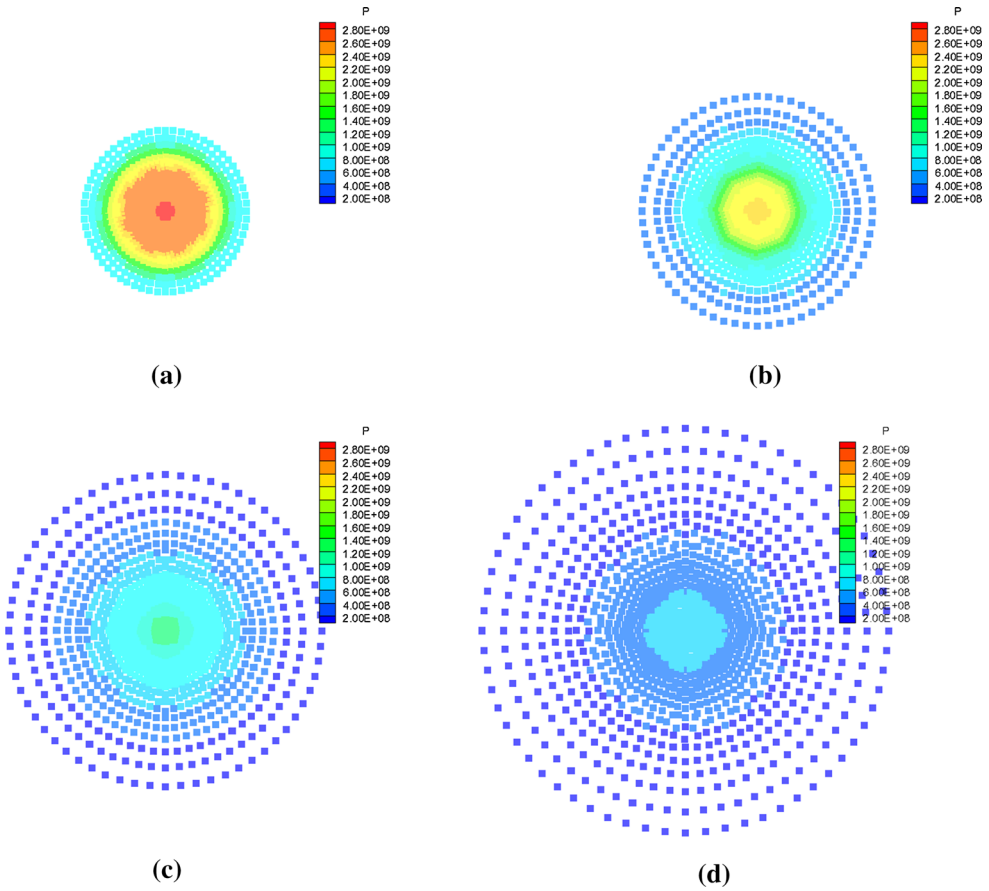

Fig. 7 The time sequences of the expansion of the TNT gas, background:pressure (N/m^2). **a** $t = 0.025$ ms; **b** $t = 0.05$ ms; **c** $t = 0.075$ ms; **d** $t = 0.10$ ms

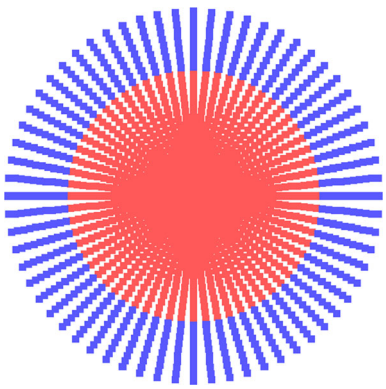

Fig. 8 The peridynamics and SPH coupling domain

Table 3 The material parameters (DP model) used for adobe

E	ν	ϕ	ψ	c	ρ	β
98,454,200 Pa	0.25	0.738663	0.738663	208,848 Pa	1,300 kg/m^3	−1

Table 4 The parameters of artificial viscosity for soil

α_Π	β_Π	ϕ
1.0	5.0	0.1

In the second example, we consider a ring of soil material that encompasses a cylinder of explosive gas. We hope to simulate the dynamic interaction between the soil and explosive gas after the detonation. Again because of the axisymmetry of the domain, we can treat this as a two-dimensional problem.

This numerical simulation was carried out to test the proposed peridynamics–SPH coupling equations and the peridynamics DP model in finite deformation. In this simulation, the cylinder explosive gas from the previous example is surrounded with a soil (adobe) ring, as shown in Fig. 8. Here, the red particles represent the explosive gas, and the blue particles represent the soil. The radius of the whole domain is 0.15 m. This domain is discretized into 640 DP node-based peridynamic particles (the soil ring) and 1,057 SPH particles (the explosive gas).

The material parameters for the explosive are the same as those used in the previous example. The time step used in the simulation is $\Delta t = 5.0 \times 10^{-7}$ s. In [38], a series of

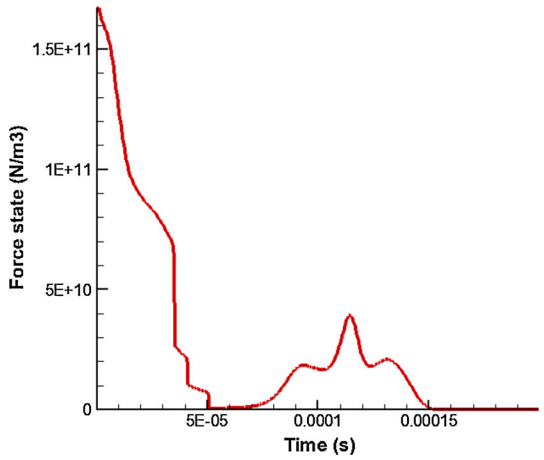

Fig. 9 The interaction force state between soil and gas

tests were conducted to calibrate the material parameters of the DP model for adobe material. Thus in the simulation, the material parameters of the soil are chosen to be exactly the same as those in [38] with an exception of the density of adobe, which is set as common (commercial) adobe material, as shown in Table 3.

Notice that the artificial viscosity model (Eq. (9)) is implemented here to help catch the blast wave front as well as to prevent non-physical penetrations. In practice, the values of the parameters are chosen from Table 4. These values render robust computation in the simulation.

With the expansion of the explosive gas, enormous pressure will be imposed on the adjacent soil media thus driving the movement of the soil. As described in Sect. 4, both the peridynamics and SPH kernels can cross the soil–gas interface, which implies that the interaction effect is involved in numerical summations of these two types of particles. The peridynamics method constructs a novel equation using the force state vectors, T_i, to represent the interaction between two particles.

Consider a particle next to the explosive gas along the radial direction/axis. Because the whole domain is axisymmetric, the force state vector only depends on coordinates r and z. This particle can have two types of bonds, ones that are associated with the peridynamic particles, and ones that are associated with SPH particles, respectively. To illustrate the soil–gas interaction effect, the sum of the force states (T_r) of the given particle is plotted in Fig. 9 at different time instances, i.e.,

$$\mathbf{T}_r = \sum_{B \in \mathcal{H}_{\mathbf{X}^A}} (\mathbf{T}_A - \mathbf{T}_B) \Delta V^B \qquad B \in \text{SPH} \tag{59}$$

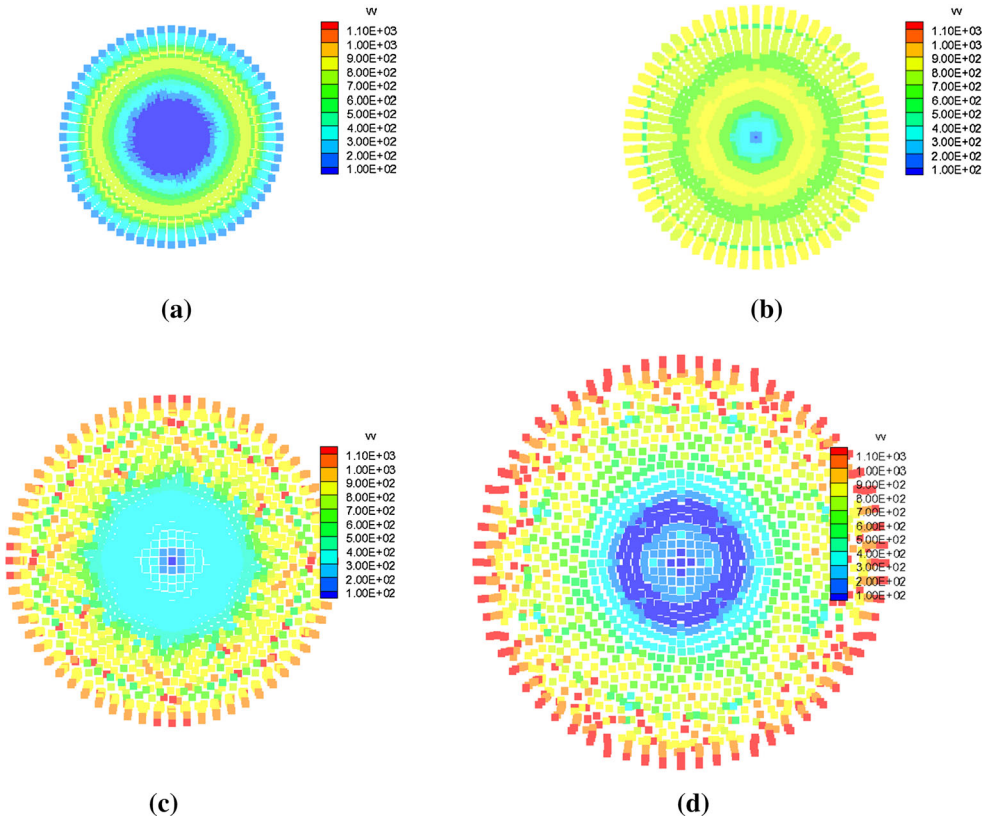

Fig. 10 The time sequences of the soil ring with explosive gas, background:velocity (m/s). bfa $t = 0.025$ ms; **b** $t = 0.075$ ms **c** $t = 0.125$ ms; **d** $t = 0.175$ ms

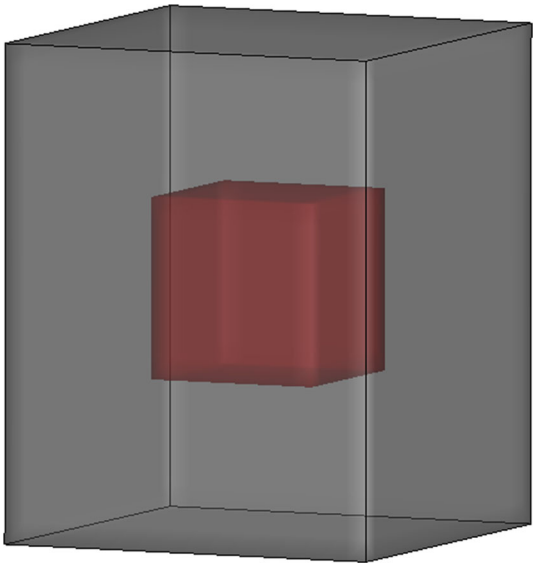

Fig. 11 The computation domain for 3D fragmentation

Note that this peridynamic particle is attached to adjacent SPH particles as well as peridynamic particles.

In Fig. 9, a sharp pulse load representing the shock wave front is generated at the very beginning. This is followed by a smaller pulse load representing dynamic oscillation between different media, which is typical in shock wave propagation. This observation indicates that the proposed peridynamics–SPH coupling method can capture shock wave propagation. Comparing the pressure evolution of the explosive gas in this simulation with what is tested in the previous example, one can see that the dynamic motion of the soil and explosive gas is consistent. Thus we conclude that the soil–gas interaction force computed here is reasonable.

The dynamic responses of the soil ring with the explosive gas are shown in Fig. 10. Here we can see that the soil particles move consistently and convectively along with the expansion of the explosive gas. In the numerical simulations, we did not find non-physical or incompatible gas penetration. These usually occur when a numerical algorithm fails to capture

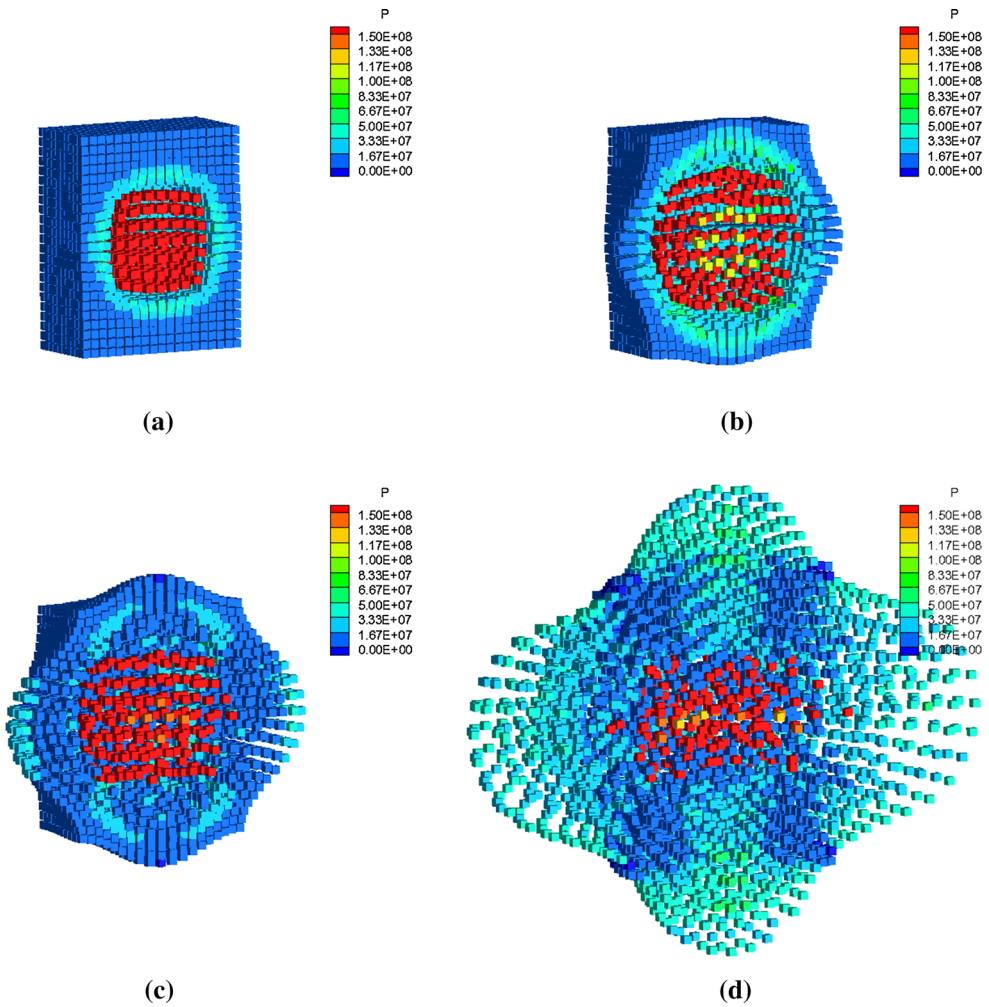

Fig. 12 The time sequence of fragmentation of adobe block. Background: pressure. **a** $t = 0.09$ ms; **b** $t = 0.25$ ms; **c** $t = 0.37$ ms; **d** $t = 0.70$ ms

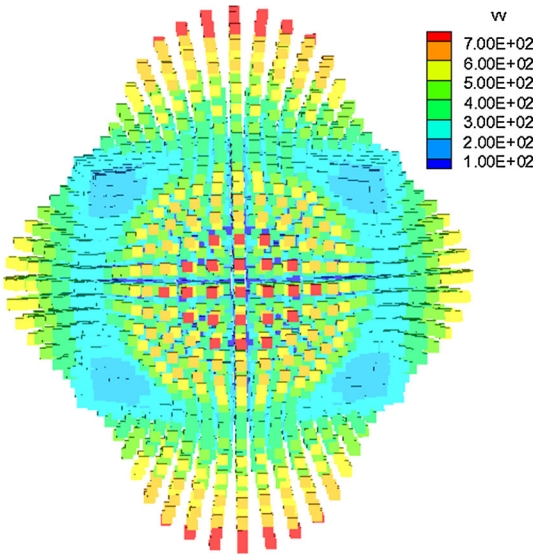

Fig. 13 The fragmentation of soil induced by blast wave

the soil–gas interaction and shock wave propagation. This confirms that the artificial viscosity stress term works well.

6.3 Fragmentation of a 3D soil block induced by shock wave load

In the last example, we consider a 3D soil–gas interaction problem where the explosive is originally buried or embedded at the center of a cubic soil block.

In this example, a preliminary numerical simulation is conducted to test the capability of the peridynamics–SPH coupling equations in capturing the complex fragmentation process of soil under blast wave loads. The motivation of this simulation is to predict ejection of soil induced by the shock wave loading that is generated by the buried explosives. To simplify this problem, the computational specimen is designed as a soil block with a buried cubic void as shown in Fig. 11. The soil block has dimensions of $0.37 \times 0.37 \times 0.47\,\mathrm{m}^3$ with a $0.123 \times 0.123 \times 0.13\,\mathrm{m}^3$ void block inside representing the explosive gas. The whole domain is discretized into 8,303 particles, consisting of 7,960 peridynamic particles and 343 SPH particles. The material parameters of the soil DP model are the same as those used in the previous example.

The dynamic fracture process of the soil block is depicted in Fig. 12. In this work, we focused on the technical issues of the peridynamics–SPH coupling. In this example, a preliminary test for the 3D simulation of fragmentation is presented. Its quantitative validation will be conducted in future work. A time sequence of the explosion with the velocity background at $t = 0.57\,\mathrm{ms}$ is shown in Fig. 13. One can see that the fragment zones (red color) are generated from what was initially a continuous body.

7 Conclusions

The numerical simulations of fragmentation in geomaterials under a high strain rate blast wave involve challenges such as representing the discontinuity inside the material, generating the explosive loading, and capturing the soil–gas interaction. In this paper, we present a novel technique that couples peridynamics with smoothed-particle hydrodynamics (SPH). Peridynamics offers an efficient method to model geomaterials, and SPH offers and efficient method to model explosive gas.

The numerical results reported in this work have shown that the proposed model is capable of simulating the complex fragmentation process of soil driven by the shock wave and buried explosive. The main technical contributions of this work include: (1) a peridynamics model of soil with artificial viscosity. This allows us to capture the moving shock wave front and to prevent non-physical penetration in numerical simulations; (2) a simple interaction technique that can transfer dynamic loads from the explosive gas to the soil, and (3) a ghost particle technique to enrich the peridynamics approximation field both near the domain boundary as well as the fracture surfaces of the geomaterial. Overall, this technique can significantly improve the accuracy of the peridynamics approximation near the boundary of the simulation domain.

Finally, several numerical simulations were carried out to test the proposed peridynamics–SPH approach. The simulation results have shown that the proposed peridynamics–SPH coupling approach can qualitatively capture the dynamic response and fracture/fragmentation process of soil under shock wave loading.

Acknowledgments This work was supported by an ONR MURI Grant N00014-11-1-0691. This support is gratefully acknowledged. In addition, Mr. Houfu Fan would like to thank the Chinese Scholarship Council (CSC) for a graduate fellowship.

References

1. Madenci E, Oterkus E (2014) Peridynamic theory and its applications. Springer, New York
2. Silling SA (2000) Reformulation of elasticity theory for discontinuities and long-range forces. J Mech Phys Solids 48:175–209
3. Bobaru F, Hu W (2012) The meaning, selection, and use of the peridynamics horizon and its relation to crack branching in brittle materials. Int J Fract 176:215–222
4. Gerstle W, Sau N, Silling S (2007) Peridynamics modeling of concrete structures. Nucl Eng Des 237:1250–1258
5. Askari A, Xu J, Silling S (2006) Peridynamics analysis of damage and failure in composites. In: 44th AIAA aerospace sciences meeting and exhibit. Reno, Nevada, AIAA-2006-88
6. Kilic B, Madenci E, Ambur DR (2006) Analysis of brazed single-lap joints using the peridynamics theory. In: 47th AIAA/ASME/ASCE/AHS/ASC structures, structural dynamics, and materials conference. Newport, Rhode Island, AIAA-2006-2267

7. Silling SA, Askari E (2004) Peridynamics modeling of impact damage. In: Moody FJ (ed) Problems involving thermal-hydraulics, liquid sloshing, and extreme loads on structures, vol 489, PVPAmerican Society of Mechanical Engineers, New York, pp 197–205
8. Silling SA, Epton M, Weckner O, Xu J, Askari E (2007) Peridynamics states and constitutive modeling. J Elast 88:151–184
9. Silling SA, Lehoucq RB (2008) Convergence of peridynamics to classical elasticity theory. J Elast 93:13–37
10. Tupek MR, Rimoli JJ, Radovitzky R (2013) An approach for incorporating classical continuum damage models in state-based peridynamics. Comput Methods Appl Mech Eng 263:20C26
11. Warren TL, Silling SA, Askari E, Weckner O, Epton MA, Xu J (2009) A non-ordinary state-based peridynamics method to model solid material deformation and fracture. Int J Solids Struct 46(5):1186–1195
12. Foster JT, Silling SA, Chen WW (2010) Viscoplasticity using peridynamics. Int J Numer Methods Eng 81:1242–1258
13. Wecknera O, Mohamed NAN (2009) Viscoelastic material models in peridynamics. Appl Math Computat 219(11):6039–6043
14. Tuniki BK (2012) Peridynamics constitutive model for concrete. Master thesis, Dept. of Civil Engineering, University of New Mexico, NM USA
15. Vermeer PA, Borst R (1984) Non-associated plasticity for soils, concrete, and rock. Heron 29(3):3–64
16. Matsuoka H, Nakai T (1974) Stress-deformation and strength characteristics of soil under three different principal stresses. Proc Jpn Soc Civil Eng 232:59–70
17. Drucker DC, Prager W (1952) Soil mechanics and plastic analysis or limit design. Quart Appl Math 10(2):157–165
18. Lammi CJ, Vogler TJ (2012) Mesoscale simulations of granular materials with peridynamics. Shock compressison of condensed matter-2011. Proceedings of the conference of the American Physical Society Topical Group on shock compression of condensed matter, vol 1426, pp 1467–1470
19. Lammi CJ, Zhou M (2013) Peridynamics simulation of inelasticity and fracture in pressure-dependent materials. The workshop on nonlocal damage and failure: peridynamics and other nonlocal models. San Antonio, TX
20. Alia A, Souli M (2006) High explosive simulation using multimaterial formulations. Appl Therm Eng 26:1032C1042
21. Gingold RA, Monaghan JJ (1977) Smoothed particle hydrodynamics—theory and application to non-spherical stars. Mon Not R Astron Soc 181:375–389
22. Liu GR, Liu MB (2003) Smoothed particle hydrodynamics: a meshfree particle method. World Scientific, Singapore
23. Belytschko T, Liu WK, Moran B (2000) Nonlinear finite elements for continua and structures. Wiley, Chichester, UK
24. Ren B, Li SF (2013) A three-dimensional atomistic-based process zone model simulation of fragmentation in polycrystalline solids. Int J Numer Methods Eng 93:989–1014
25. Liu WK, Jun S, Zhang YF (1995) Reproducing kernel particle methods. Int J Numer Methods Fluids 20:1081–1106
26. Ren B, Li SF (2010) Meshfree simulations of plugging failures in high-speed impacts. Comput Struct 88:909–923
27. Liu WK, Hao S, Belytschko T, Li S, Chang CT (2000) Multi-scale methods. Int J Numer Methods Eng 47(7): 1343–1361
28. Chen X, Gunzburger M (2011) Continuous and discontinuous finite element methods for a peridynamics model of mechanics. Comput Methods Appl Mech Eng 200:1237C1250
29. Li S, Liu WK (2004) Meshfree particle methods. Springer, Berlin
30. von Neumman J, Richtmyer RD (1950) A method for the numerical calculation of hydrodynamic shocks. J Appl Phys 21:232–247
31. Monaghan JJ (1989) On the problem of penetration in particle methods. J Computat Phys 82:1–15
32. Ren B, Li SF (2012) Modeling and simulation of large-scale ductile fracture in plates and shells. Int J Solids Struct 49:2373–2393
33. Bessa MA, Foster JT, Belytschko T, Liu WK (2014) A meshfree unification: reproducing kernel peridynamics. Computat Mech 53(6):1251–1264
34. Li S, Liu WK (1999) Reproducing kernel hierarchical partition of unity Part I—formulation and theory. Int J Numer Methods Eng 45(3):251–288
35. Libersky LD, Petscheck AG, Carney TC, Hipp JR, Allahdadi FA (1993) High strain Lagrangian hydrodynamics—a three dimensinoal SPH code for dynamic material response. J Computat Phys 109:67–75
36. Monaghan JJ (1994) Simulating free surface flow with SPH. J Computat Phys 110(2):399–406
37. Campbell PM (1988) Some new algorithms for boundary values problems in smoothed particle hydrodynamics. Defence Nuclear Agency (DNA) report DNA-88-286
38. Torres LQ (2012) Assessment of the applicability of nonlinear Drucker–Prager model with cap to adobe. 15th world conference on earthquake engineering (WCEE), Lisboa, Portugal
39. Han LH, Elliott JA, Bentham AC, Mills A, Amidon GE, Hancock BC (2008) A modified Drucker–Prager cap model for die compaction simulation of pharmaceutical powders. Int J Solids Struct 45:3088–3106
40. Zienkiewicz OC, Chan AHC, Pastor M, Schrefler BA, Shiomi T (1999) Computational geomechanics with special reference to earthquake engineering. Wiley, Chichester, UK
41. Hughes TJR, Winget J (1980) Finite rotation effects in numerical integration of rate constitutive equations arising in large-deformation analysis. Int J Numer Methods Eng 15(12): 1862–1867